 doi:10.20944/preprints202105.0470.v1

Article

Fracture and size effect of PFRC specimens simulated by using a trilinear softening diagram: a predictive approach

F. Suárez [1], J.C. Gálvez [2]*, M.G. Alberti [2] and A. Enfedaque [2]

[1] Departamento de Ingeniería Mecánica y Minera, Universidad de Jaén, 23071 Jaén, Spain; fsuarez@ujaen.es
[2] Departamento de Ingeniería Civil-Construcción, Universidad Politécnica de Madrid, E.T.S.I. Caminos, Canales y Puertos, 28040 Madrid, Spain
* Correspondence: jaime.galvez@upm.es; Tel.: +034-910-674-125

Abstract: Size effect on plain concrete specimens is well known and can be correctly captured when performing numerical simulations by using a well characterised softening function, but in the case of fibre reinforced concrete this is not directly applicable, since an only diagram cannot capture the material behaviour on elements with different size due to dependence of the orientation factor of the fibres with the size of the specimen. In previous works, the use of a trilinear softening diagram proved to be very convenient for reproducing fracture of polyolefin fibre reinforced concrete elements, but only if it is previously adapted for each specimen size. In this work, a predictive methodology is used to reproduce fracture of polyolefin fibre reinforced concrete specimens of different sizes under three-point bending. Fracture is reproduced by means of a well known embedded cohesive model, with a trilinear softening function that is defined specifically for each specimen size. The fundamental points of these softening functions are defined *a priori* by using empirical expressions proposed in past works, based on an extensive experimental background. Therefore, the numerical results are obtained in a predictive manner, and then compared with a previous experimental campaign, showing that this approach properly captures the size effect, although some values of the fundamental points in the trilinear diagram could be defined more accurately.

Keywords: Size effect; Polyolefin fibre reinforced concrete; Trilinear softening function; Cohesive model

1. Introduction

In the case of plastic limit analysis or elasticity assessed up to a strength limit, results are independent of the specimen size, but in the case of elements made of quasi-brittle materials, such as concrete, evaluated beyond the proportionality limit, the nominal strength is dependent on the specimen size.

Size effect on plain concrete is well known and is the reason why when the size of a concrete specimen increases keeping the same proportions, fracture develops at lower values of the nominal strength [1]. When fracture in plain concrete is numerically reproduced, size effect can be correctly captured by means of a cohesive zone formulation that uses a well characterised softening diagram [2–4]. In fact, as Bažant states, the cohesive crack model proposed by Hillerborg can be considered as the most realistic among simple models when quasi-brittle fracture is studied [5].

On another note, polyolefin fibre reinforced concrete (PFRC) is experiencing a great development in the last years, due to its good mechanical behaviour and the fact that it reduces and, in some cases, even eliminates some of the problems observed in steel fibre reinforced concrete (SFRC) such as corrosion, sensitivity to magnetic fields or wear and tear of machinery related to its production (concrete pumps and mixers, for example), making PFRC particularly suitable for some uses. Although this material is starting to count with initial examples of use as a structural material [6,7], one of the reasons why

Preprints (www.preprints.org) | NOT PEER-REVIEWED | Posted: 20 May 2021 doi:10.20944/preprints202105.0470.v1

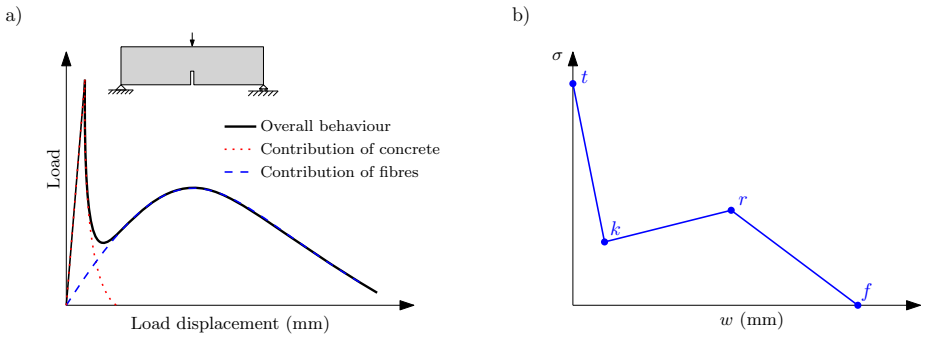

Figure 1. a) Load-displacement diagram obtained in a three-point bending test with a PFRC specimen, b) Trilinear softening diagram.

PFRC is still not becoming as widespread as it could is probably the scarce experience with it and the uncertainty on its behaviour in real engineering works under certain situations. One of the aspects that must be clarified is the size effect, this is of paramount importance if the material properties measured at a laboratory scale are to be used for designing larger structures.

There is not much information about size effect in fibre reinforced concrete (FRC), especially in the case of PFRC, given that it is a relatively recent material. In the case of SFRC, some studies can be found [8,9] and in the case of PFRC, an experimental campaign has been recently carried out [10], which has shown that the nominal strength at the limit of proportionality is governed by the matrix (concrete) and the post-cracking residual strength is governed by the fibres.

In previous works, the use of a cohesive zone formulation fed with a trilinear softening curve has proved to be very convenient for reproducing the fracture process in FRC [11], but it must be adapted depending on several factors such as the fibre length, the fibre proportion [12] and the specimen size [13]. This trilinear softening diagram describes the contribution of matrix and fibres in the fracture process which, due to the different elastic moduli of both materials, begin to significantly work at different stages of load transmission. Considering the trilinear diagram shown in Fig. 1, the initial point t identifies the fracture of the concrete matrix, k the point at which the contribution of fibres starts to predominate over the contribution of the matrix, r the maximum remanent contribution of fibres and f the eventual failure of the material.

In [12] some parameters of the PFRC mix were identified and some expressions were also proposed to define the fundamental points of the trilinear diagram (k and r points). In addition to this, in [14] the length and orientation of fibres were observed as key parameters to define the trilinear diagram, also identifying a higher threshold of the PFRC behaviour obtained testing specimens with long fibres oriented in the optimum direction.

From the numerical point of view, there exist many approaches and models that help simulating fracture. In many cases, these models are calibrated using the experimental results of the test simulated, but this does not guarantee that the parameters represent any other case different from the one under study. From this point of view, the most interesting approach consists of finding models that can reproduce fracture in a predictive way, that is to say, a model that is fed with parameters obtained by experimental tests that are different from the loading case that wants to be simulated. This type of models are considered as less biased and more representative of the material, not of a specific loading case.

The main aim of this contribution is to reproduce fracture on different size specimens of PFRC using a predictive approach. A cohesive model and a softening diagram that corresponds to a trilinear function defined *a priori* is employed. Using the knowledge obtained in previous works, the coordinates of each of the fundamental points t, k, r and f are identified. To do this, the experimental results of [10] are reproduced

Preprints (www.preprints.org) | NOT PEER-REVIEWED | Posted: 20 May 2021 doi:10.20944/preprints202105.0470.v1

Table 1: Fibres properties.

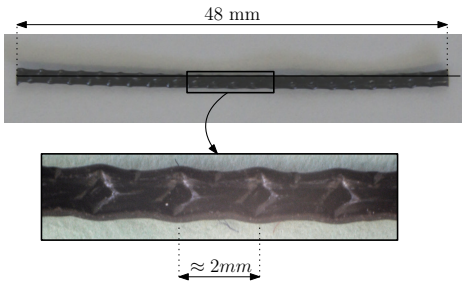

Material density (g/cm^3)	0.910
Eq. diameter (mm)	0.903
Tensile strength (MPa)	>500
Modulus of elasticity (GPa)	>9

and compared through a finite element analysis by using an embedded cohesive crack formulation. In the following sections, the experimental work used as reference of the size effect in PFRC is briefly described, then the main features of the embedded cohesive crack model used to numerically reproduce fracture are presented and the trilinear softening functions used with each specimen size obtained by means of the expressions proposed in [12]. Since, as will be later discussed, some parameters of the diagram (more specifically w_r and w_f) are estimated, some parts of the load-displacement curves obtained numerically only agree partially with the experimental results. Therefore, in the final part of this paper, an analysis of the influence of such parameters is be carried out and some conclusions highlighted.

2. Experimental benchmark

In order to compare the numerical simulations with experimental results, the campaign described in [10] is used. For a detailed description of this campaign, the reader is encouraged to read the referenced work, since here only the main aspects relevant for the present study are presented.

Concrete reinforcement consists of 48 mm long polyolefin macrofibres with embossed surface. The main properties of these fibres can be consulted in Table 1. More information on these fibres can be found in [15].

The experimental campaign of reference involved three-point bending tests carried out following the guidelines of the EN-14651 standard [16] (except for the specimen sizes and notch dimensions). Figure 2 shows a schematic drawing of the experimental setup and Table 2 the specimens dimensions. In all cases, the concrete composition was the same and 48 mm long polyolefin fibres were used in a proportion of 10 kg/m^3.

In these tests, the load and the displacement were obtained from the testing machine and the evolution of the crack mouth opening displacement (CMOD) was measured by means of a digital image correlation system (DIC). To compare the experimental results, two main diagrams were employed: load versus displacement of the application point of the load and load versus CMOD. Figure 2 shows these values over the scheme of a damaged specimen during the test.

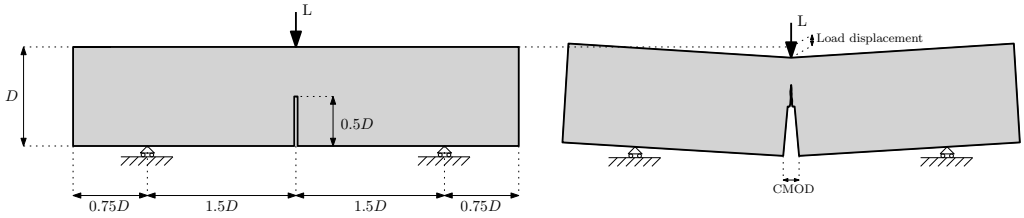

Figure 2. Left: scheme of a three-point bending test and specimen geometry. Right: scheme of a damaged specimen during the test.

Preprints (www.preprints.org) | NOT PEER-REVIEWED | Posted: 20 May 2021 doi:10.20944/preprints202105.0470.v1

Table 2: Specimens dimensions.

Specimen	Length (mm)	Width (mm)	Height (mm)	Notch (mm)
Large	1350	50	300	150
Medium	675	50	150	75
Small	340	50	75	37.5

3. Embedded cohesive crack model

The crack process is modelled by using the finite element analysis and adapting a formulation based on the cohesive zone approach developed by Hillerborg [17], inspired by the work of Dugdale [18] and Barenblatt [19]. This formulation simulates fracture inside an element using the strong discontinuity approach and was initially developed for concrete [20,21], but later adapted to brickwork masonry elements [22] and fibre-reinforced cementitious materials [11–13].

The cohesive zone approach relies on the experimental evidence that fracture usually develops under a predominant local mode I. Thus, this approach assumes that the cohesive stress vector $\boldsymbol{t}$ is perpendicular to the crack opening and parallel to the crack displacement vector $\boldsymbol{w}$, which is expressed by (1).

$$\boldsymbol{t} = \frac{f(\tilde{w})}{\tilde{w}}\boldsymbol{w} \qquad \text{with } \tilde{w} = \max(|\boldsymbol{w}|) \tag{1}$$

where $f(|\tilde{w}|)$ stands for the material softening function, defined in terms of an equivalent crack opening $\tilde{w}$. This equivalent crack opening stores the maximum historical crack opening to account for possible unloading scenarios. In this case, the softening diagram is defined as trilinear, as shown in Fig. 3, and the load-unload branches follow lines towards the origin in all cases. The trilinear diagram is defined by the following expression:

$$\sigma = \begin{cases} f_{ct} + \left(\dfrac{\sigma_k - f_{ct}}{w_k}\right) \cdot w & \text{if } 0 < w \leq w_k \\ \sigma_k + \left(\dfrac{\sigma_r - \sigma_k}{w_r - w_k}\right) \cdot (w - w_k) & \text{if } w_k < w \leq w_r \\ \sigma_r + \left(\dfrac{-\sigma_r}{w_f - w_r}\right) \cdot (w - w_r) & \text{if } w_r < w \leq w_f \\ 0 & \text{if } w > w_f \end{cases} \tag{2}$$

In the finite element models presented later, the embedded cohesive crack formulation is used with constant strain triangular elements. Cracking can only develop in three directions, each parallel to the element sides and at mid height, which guarantees that local and global equilibria are satisfied. Fig. 4 shows the only three possible crack paths in an element.

Once the crack direction is defined, the element is divided into two parts, A^+ and A^- and the stress vector $\boldsymbol{t}$ is constant along the crack, expressed by (3).

$$\boldsymbol{t} = \frac{A}{hL}\boldsymbol{\sigma} \cdot \boldsymbol{n} \tag{3}$$

where A stands for the area of the element, h for the height of the triangle over the side opposite to the solitary node, L for the crack length in the element and $\boldsymbol{n}$ for the unit vector normal to that side and to the crack. Since crack is parallel to one side of the triangular element and is placed at midheight, expression 3 turns into $\boldsymbol{t} = \boldsymbol{\sigma} \cdot \boldsymbol{n}$ (the reader can find more details of this and other aspects of the model in [20]).

The material outside the crack is assumed to be elastic and the crack displacement vector $\boldsymbol{w}$ is solved considering that the stress tensor can be obtained by substracting an

Preprints (www.preprints.org) | NOT PEER-REVIEWED | Posted: 20 May 2021 doi:10.20944/preprints202105.0470.v1

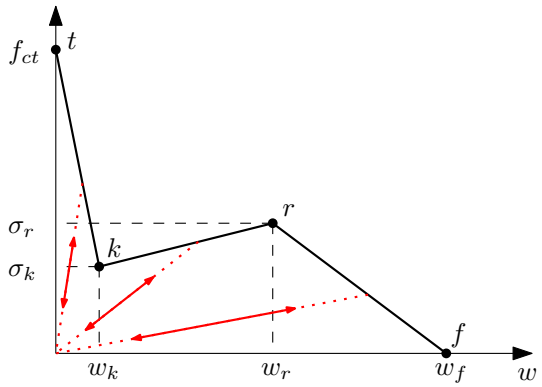

Figure 3. Scheme of a trilinear softening function. Load-unload branches follow a line towards the origin.

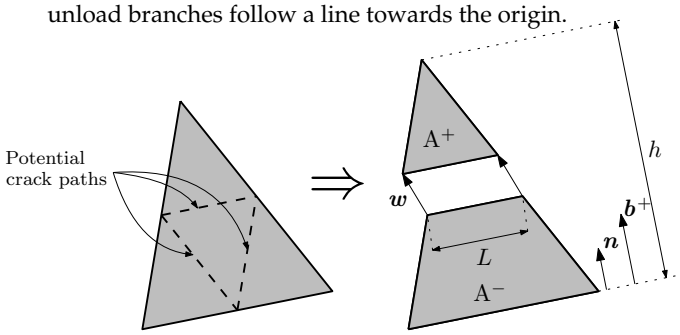

Figure 4. Potential crack paths (left) and geometrical definitions of $\boldsymbol{w}$, $\boldsymbol{n}$ and $\boldsymbol{b}^+$ (right).

inelastic part, which considers the contribution of the crack displacement, to the elastic prediction computed using the apparent strain by means of (4).

$$\boldsymbol{\sigma} = \boldsymbol{E} : \left[\epsilon^a - \left(\boldsymbol{b}^+ \otimes \boldsymbol{w}\right)^S\right] \cdot \boldsymbol{n} \tag{4}$$

where $\boldsymbol{E}$ is the elastic tangent tensor, ϵ^a the apparent strain vector obtained with the nodal displacements, $\boldsymbol{b}^+$ the gradient vector of the shape function that corresponds to the solitary node, which can be easily obtained in this case by (5), superscript S indicates the symmetric part of the resulting tensor, : the double-dot product ($(\boldsymbol{A} : \boldsymbol{b})_{ij} = A_{ijkl} b_{kl}$) and $\otimes$ the direct product ($(\boldsymbol{a} \otimes \boldsymbol{b})_{ij} = a_i b_j$).

$$\boldsymbol{b}^+ = \frac{1}{h}\boldsymbol{n} \tag{5}$$

In order Since the stress vector $\boldsymbol{t}$ can be obtained as $\boldsymbol{t} = \boldsymbol{\sigma} \cdot \boldsymbol{n}$, using the expression of $\boldsymbol{\sigma}$ obtained with (4) and the expression of $\boldsymbol{t}$ in terms of the crack opening (1):

$$\frac{f(\tilde{w})}{\tilde{w}}\boldsymbol{w} = \left[\boldsymbol{E} : \boldsymbol{\epsilon}^a\right] \cdot \boldsymbol{n} - \left[\boldsymbol{E} : \left(\boldsymbol{b}^+ \otimes \boldsymbol{w}\right)^S\right] \cdot \boldsymbol{n}$$

which can be rewritten as:

$$\left[\frac{f(\tilde{w})}{\tilde{w}}\boldsymbol{1} + \boldsymbol{n} \cdot \boldsymbol{E} \cdot \boldsymbol{b}^+\right] \cdot \boldsymbol{w} = \left[\boldsymbol{E} : \boldsymbol{\epsilon}^a\right] \cdot \boldsymbol{n} \tag{6}$$

where $\boldsymbol{1}$ stands for the second-order identity tensor. Using an iterative process (such as the Newton-Raphson method), the crack displacement w that satisfies (6) can be obtained.

This model is implemented using a UMAT subroutine in ABAQUS and, since vectors $\boldsymbol{n}$, $\boldsymbol{b}^+$, crack length L and the element area A are computed using the nodal coordinates for each element, it reads an external file with this information.

Preprints (www.preprints.org) | NOT PEER-REVIEWED | Posted: 20 May 2021 doi:10.20944/preprints202105.0470.v1

4. Definition of the trilinear softening diagrams

As observed in [12], there are several parameters that can be experimentally measured and help to define the trilinear diagram for the PFRC. Apart from the fracture parameters of plain concrete (G_F and f_t), which define the first part of the diagram, these parameters are the volume of fibres (V_f), the orientation factor (θ) and the percentage of pulled out fibres at the fracture surface ($\%Pulled-out$). With the help of V_f, the angle ϕ can be obtained by means of (7).

$$\phi = -3.6046 + 5.0625 \cdot \left(1 - e^{(-6.55 \cdot V_f)}\right) \tag{7}$$

This angle serves to identify the second point of the diagram (point k), which is the intersection of the softening function of plain concrete (here considered as an exponential function: $\sigma = f_t \cdot \exp(-\frac{f_t \cdot w}{G_F})$) with a line passing through the origin with a direction defined by ϕ (see Fig. 5).

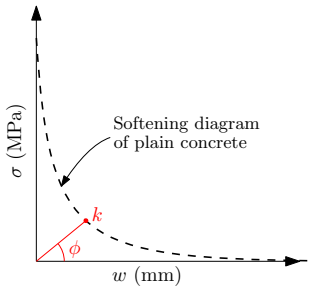

Figure 5. Identification of k point of the trilinear diagram by means of the ϕ angle.

By using the three main parameters mentioned before and the ultimate tensile strength of the fibres (σ_u), the maximum remaining strength (σ_r) can be obtained with (8)

$$\sigma_r = (1 - \%Pulled-out) \cdot V_f \cdot \theta \cdot \sigma_u \tag{8}$$

Considering the scheme of the trilinear diagram shown in Fig. 1, the first two points can be identified as follows: point t is identified by f_t, which can be experimentally obtained, point k depends on the volume fraction of fibres (V_f) by means of the ϕ angle defined with (7) and the softening function of plain concrete, Table 3 shows the intermediate values that result of this calculation.

Table 3: Intermediate values for obtaining point k of the trilinear diagram.

	f_t (MPa)	G_F (N/mm)	ϕ	w_k (mm)	σ_k (MPa)
Small/Medium/Large	3.2	0.13	1.448	0.07143	0.57715

As regards the remaining two points, r and f, the value of σ_r can be obtained with (8) (Table 4 shows the results of this calculation for each size) and σ_f is, obviously, equal to 0, but w_r and w_f must be estimated; they depend on the fibre length but there are no specific expressions to obtain them. In this case, w_r is estimated as equal to 1.65 mm, since this was the value adopted in [13] for simulating fracture in specimens made with 48 mm long fibres of the same kind as those used here. As regards w_f, this value is related to the maximum crack opening before completely losing the bonding between the fibres and the matrix, therefore it is assumed to be proportional to the fibre length. Thus, since in [12] specimens made with 60 mm long fibres were modelled using $w_f = 7.5$ mm, here a value of $w_f = \frac{48}{60} \cdot 7.5 = 6.0$ mm is adopted. Figure 6 shows the resulting trilinear softening diagrams for all three sizes.

Preprints (www.preprints.org) | NOT PEER-REVIEWED | Posted: 20 May 2021 doi:10.20944/preprints202105.0470.v1

Table 4: Intermediate values for obtaining σ_r for all three considered sizes.

	θ	$\%Pulled-out$	V_f	σ_u (MPa)	σ_r (MPa)
Small	0.63	0.54	0.011	376	1.20
Medium	0.62	0.54	0.011	376	1.18
Large	0.72	0.54	0.011	376	1.37

Table 5: Parameters of the softening diagrams for each specimen size.

	Small	Medium	Large
w_t (mm)	0.00	0.00	0.00
σ_t (MPa)	3.20	3.20	3.20
w_k (mm)	0.07	0.07	0.07
σ_k (MPa)	0.57	0.57	0.57
w_r (mm)	1.650	1.650	1.650
σ_r (MPa)	1.20	1.18	1.37
w_f (mm)	6.00	6.00	6.00
σ_f (MPa)	0.00	0.00	0.00

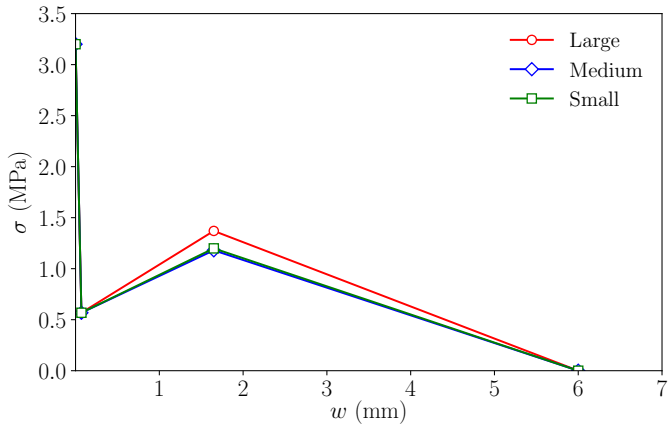

Figure 6. Initial trilinear softening diagrams.

5. Results and discussion

Fracture of the three specimen sizes analysed in [15] were carried out using the finite element method and a displacement control was used to drive the fracture evolution with a good convergence. The simulations were computed using ABAQUS [23] and fracture was reproduced by means of a UMAT subroutine that implemented the previously described material behaviour.

Figure 7 shows the three meshes used in this work with the same scale, which was refined at the region where fracture develops. In the case of the large size model (L), the side of minimum element size was around 7 mm, in the case of the medium size model (M), 3.5 mm and in the case of the small size model (S), 2 mm The refinement of these meshes was designed based on previous works (see [13]), where the mesh dependence was already analysed.

Figure 8 shows the load-load displacement and load-CMOD diagrams for all three sizes and compares them with the experimental results. Each specimen size is identified by a different colour: red for large size, blue for medium size and green for small size. The shades behind the diagrams correspond to the experimental envelopes, with the same colour code used in the diagrams. Apart from the overestimation of the initial

Preprints (www.preprints.org) | NOT PEER-REVIEWED | Posted: 20 May 2021 doi:10.20944/preprints202105.0470.v1

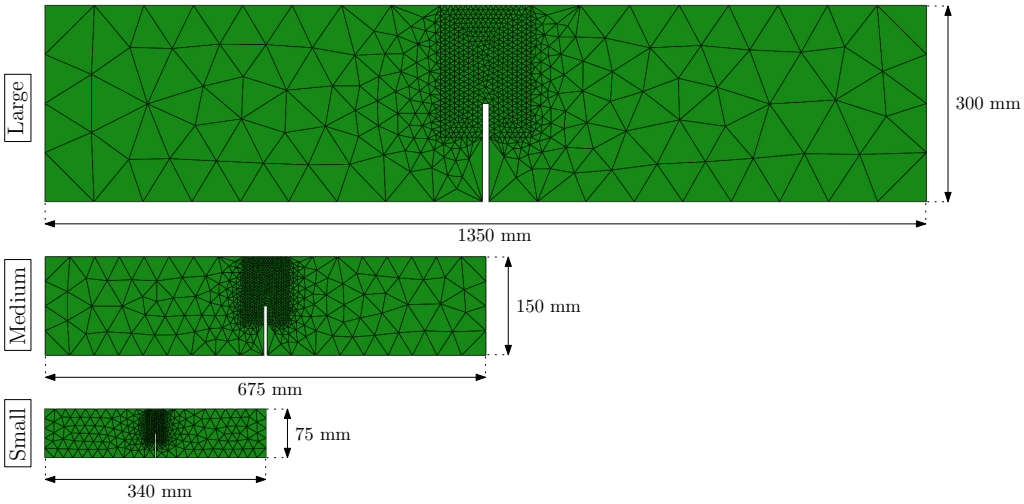

Figure 7. FEM meshes used in the simulations for each specimen size.

peak, which is a known issue when this type of numerical modelling is used, especially in large size specimens [24], the models reproduce reasonably well the experimental results. This agreement is particularly good in the case of the medium size and present some differences in the last part of the load-load displacement diagrams in the case of large and small sizes, where the numerical model tends to underestimate the specimen remaining strength.

It is also worth noting that in the case of the experimental results, the maximum remanent load takes place at a larger load displacement if compared with the medium and large sizes, while in the case of the numerical results, this maximum load after the first peak takes place approximately at the same load displacement and, in any case, following a very linear trend. These trends are depicted by dashed lines on the load-load displacement diagrams of Figure 8.

These results show that expressions 7 and 8, defined in the past by analysing the fracture behaviour of different PFRC mixes, describe well the general behavior of this material and take into account the main parameters: the volume of fibres in the mix (V_f), the orientation of fibres with respect to the fracture surface (θ) and the quality of bonding between the fibres and concrete, expressed by the fraction of fibres that are pulled out at the fracture surface ($\%Pulled-out$). Nevertheless, if the parameters used to define the trilinear softening diagrams, abscissa values of points k and f are only estimated based on previous experiences with this type of models, but there are no expressions proposed for them yet. In the following section, the influence of these two values, w_r and w_f, is studied to understand how they modify the diagrams, which can help to propose expressions to quantify them.

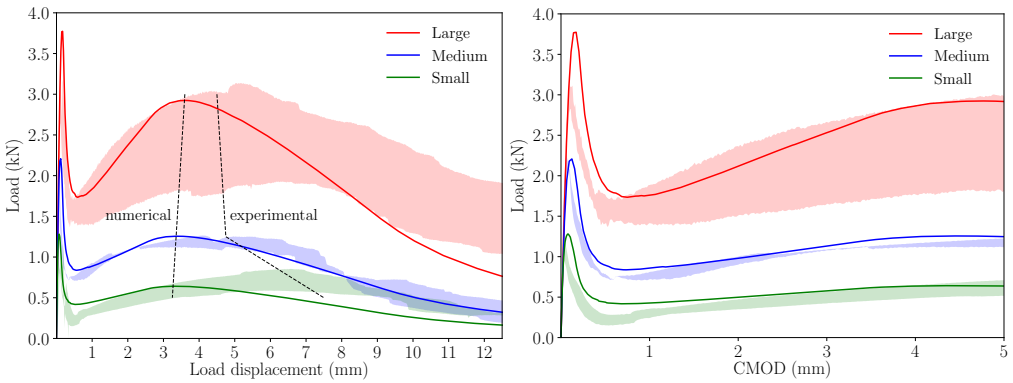

Figure 8. Numerical results compared with the experimental envelopes, each specimen size is identified by a different colour.

Preprints (www.preprints.org) | NOT PEER-REVIEWED | Posted: 20 May 2021 doi:10.20944/preprints202105.0470.v1

6. Study on the influence of w_r and w_f

6.1. Influence of w_r

To understand how the value of w_r modifies the load-load displacement and load-CMOD diagrams for each specimen size, the trilinear diagrams of Table 5 have been considered as a reference and new ones are defined by modifying the value of w_r, keeping the rest unchanged. Figure 9 shows these trilinear functions and Figure 10 the resulting load-load displacement and load-CMOD diagrams, considering the reference value of w_r, 1.65 mm, and two alternative values, 1.85 mm and 2.05 mm, identified by dashed lines and dotted lines, respectively; these values have been adopted as reasonable alternatives of the reference value according to previous experiences with this type of simulations.

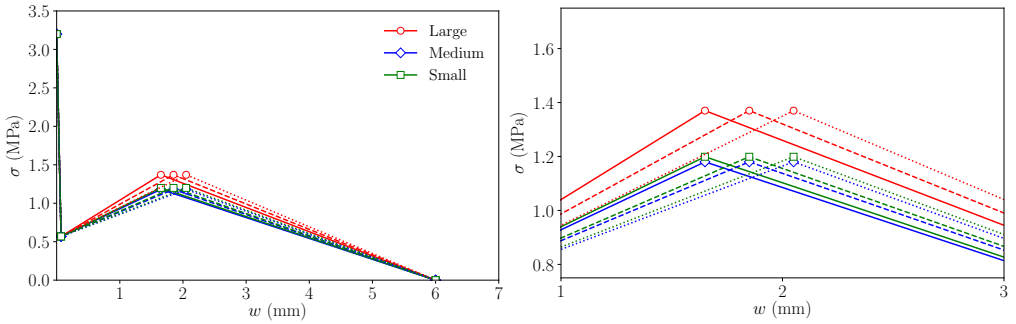

Figure 9. Left: trilinear diagrams used to study the influence of w_r on the numerical simulations; right: detail of the diagrams around point r (see Figure 3). Continuous lines represent the trilinear functions with w_r=1.65, dashed lines the functions with w_r=1.85 and dotted lines the function with w_r=2.05.

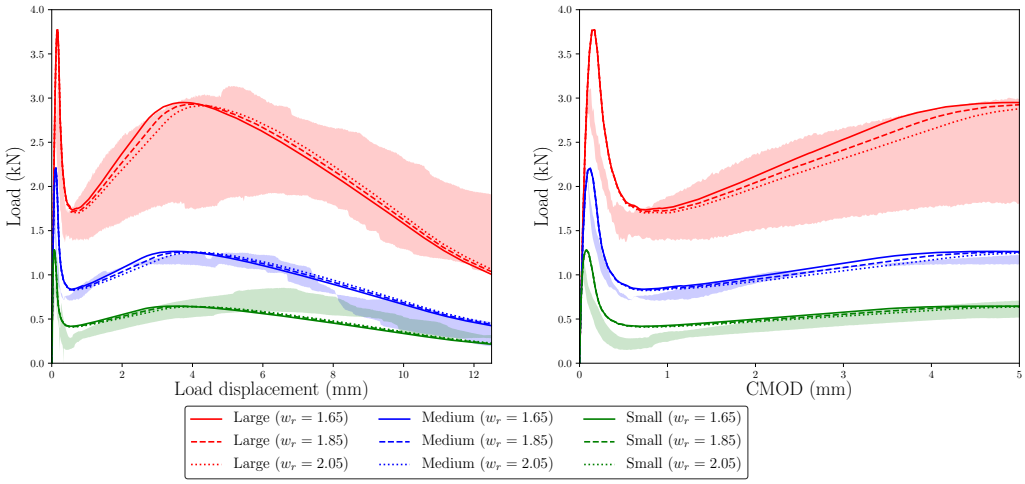

Figure 10. Numerical results compared with the experimental envelopes to study the influence of w_r on the numerical simulations. The trilinear functions used in each case are shown in Figure 9.

As a consequence of defining larger values of w_r, the maximum remanent load is reached later in the test, as could be expected, but it is also interesting to observe that the maximum load becomes slightly lower. This makes the simulations of large and medium sizes agree somewhat better with the experimental envelope. The maximum remanent load still shows proportionality with the specimen size and the experimental observation is not reproduced, since in the small size case, it still takes place earlier than in the experimental tests.

These results suggest that the value of w_r has a strong influence on the diagram, not only on the load displacement at which the maximum remanent load takes place, but

Preprints (www.preprints.org) | NOT PEER-REVIEWED | Posted: 20 May 2021 doi:10.20944/preprints202105.0470.v1

also on its value, since the larger w_r is, the smaller the maximum remanent load turns out. This is due to the uneven stress evolution along the fracture plane during the test; if w_r is smaller, the slope of the *k-r* line (see Figure 3) is steeper, therefore, the lower fibres of the fracture plane, which are the first to be damaged and the most relevant from the point of view of the bearing capacity of the section due to their position, begin to recover their loading capacity earlier. At this point, as there is a smaller fraction of the ligament damaged, the sample is capable of reaching a higher value of the remanent load before its final decay. On the contrary, if w_r is higher, the loading capacity of the lower fibres of the bearing section is recovered later, so a larger portion of the section is damaged, which leads to a smaller value of the maximum remanent load.

6.2. *Influence of* w_f

To analyse how w_f affects the fracture behaviour in the simulations of each size, the same strategy as with w_r has been followed. Using the trilinear diagrams of Table 5 as reference, two more diagrams have been created for each size by modifying only the abscissa of point f, using values considered as reasonable based on previous experiences with these simulations. Figure 11 shows these trilinear diagrams and Figure 12 the curves obtained with them in the numerical simulations.

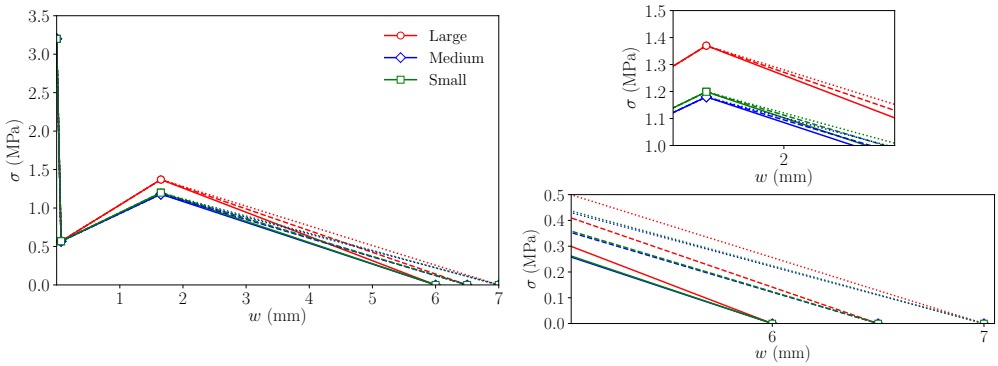

Figure 11. Left: trilinear diagrams used to study the influence of w_f on the numerical simulations; upper right: detail of the diagrams around point *r*; lower right: detail of the diagrams around point *f* (see Figure 3). Continuous lines represent the trilinear functions with w_f=6.0, dashed lines the functions with w_f=6.5 and dotted lines the function with w_f=7.0.

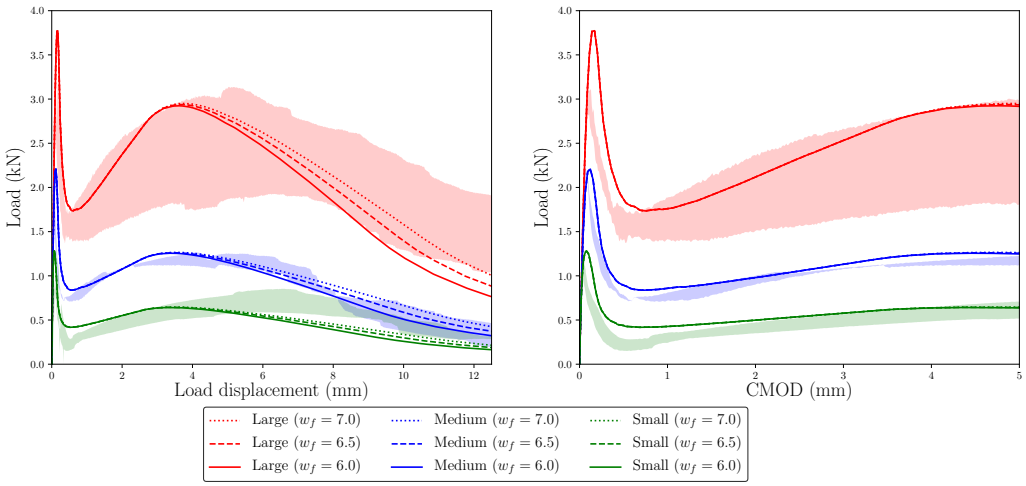

Figure 12. Numerical results compared with the experimental envelopes to study the influence of w_f on the numerical simulations. The trilinear functions used in each case are shown in Figure 11.

Preprints (www.preprints.org) | NOT PEER-REVIEWED | Posted: 20 May 2021 doi:10.20944/preprints202105.0470.v1

As expected, these diagrams show that when w_f is larger, the load decay in the last part of the test is delayed, which makes the numerical simulations more akin to the experimental observations in the case of the large size, maintaining a good agreement with the other two sizes. Although the behaviour of the model is very similar up to the maximum remanent load, there are small differences among each of the three values of w_f used in each specimen size. Taking a close look at the diagrams around the region where the maximum remanent load takes place, it can be observed that this occurs at a slightly higher value of the load displacement and the value of this load is slightly higher, although the differences are almost negligible. This behaviour is expected, since once the damage starts in the lower fibres of the ligament and progresses beyond the *r* point, their bearing capacity decays at a slower rate as the crack opens. Since the maximum remanent load is the result of a competition between the load lost by the more damaged fibres that have already reached the *r* point and the increasing bearing capacity of less damaged fibres that have still not reached the *r* point, a softer slope of the *r*-*f* line in the trilinear diagram results in a higher remanent load that takes place later in the test (see Figure 3).

Lastly, regarding the experimental trend of the maximum remanent load observed experimentally, here, again, it presents a proportional evolution with the specimen size. As observed with the alternative softening diagrams obtained by modifying w_r, the maximum remanent load occurs approximately at the same load displacement for all three sizes, while the experimental results (see the load-load displacement diagram in Figure 8) show a larger value for the small size; therefore, this aspect is not captured by the numerical simulations.

As the previous results show, modifying w_r or w_f has effect on the maximum remanent load and the final decay branch of the diagrams, but the alternative trilinear softening diagrams used suggest that these values also depend on the specimen size. Estimating w_r and w_f as fixed values for all specimen sizes result in a proportional evolution of the maximum remanent load that follow a linear trend in the load-displacement diagrams that do not agree with the experimental observations. The work carried out in past papers provide a good tool to reproduce the behaviour of PFRC elements in a predictive way, capturing reasonably well the size effect of this type of materials, but the results shown here suggest that expressions like those used to define σ_k, w_k and σ_r (see equations 7 and 8) should be found for w_r and w_f in order to have a tool that captures the whole fracture behaviour of this composite material and be fully *predictive*.

7. Conclusions

In this work, the numerical modelling of the size effect by means of a cohesive model fed with a trilinear softening function has been studied using a predictive method. A three-point bending test on specimens of three sizes have been numerically reproduced and compared with experimental data from previous works. The trilinear diagrams for each size have been defined by expressions obtained in previous experimental campaigns, resulting in good agreement with the lab observations.

From the work presented above, the following conclusions can be drawn:

1. The complete fracture behaviour of PFRC specimens can be numerically simulated using a predictive trilinear cohesive crack model, which can be defined *a priori* by means of empirical expressions obtained with lab tests different from those simulated. This diagram is defined by four points, with coordinates that depend on PFRC mechanical characteristics, i.e., the tensile strength of the matrix, the proportion of fibres and the orientation factor. Abscissa values w_r and w_f (see Figure 3) are fixed based on experimental results obtained in previous literature. It is still an unsolved challenge to obtain expressions to estimate w_r and w_f using the mechanical characteristics of the PFRC.

 doi:10.20944/preprints202105.0470.v1

2. The softening diagrams are not equal for all specimen sizes and should be adjusted for each of them. This is mainly due to a different orientation factor that varies with the size of the specimen.
3. The maximum remanent loads obtained for each size present a linear trend on the load-displacement diagram, which does not agree completely with the experimental observations, although the load-displacement and load-CMOD curves properly agree with the experimental envelopes for the three studied sizes.
4. Modifying w_r and w_f affects the maximum remanent load on the load-displacement diagram and modifies the last part of this diagram, but cannot capture the nonlinear trend of the remanent load among specimen sizes.

Acknowledgements

The authors gratefully acknowledge the financial support provided by the Ministry of Science and Innovation of Spain through the Research Fund Project PID2019-108978RB-C31.

Author Contributions: For research articles with several authors, a short paragraph specifying their individual contributions must be provided. The following statements should be used "Conceptualization, X.X. and Y.Y.; methodology, X.X.; software, X.X.; validation, X.X., Y.Y. and Z.Z.; formal analysis, X.X.; investigation, X.X.; resources, X.X.; data curation, X.X.; writing—original draft preparation, X.X.; writing—review and editing, X.X.; visualization, X.X.; supervision, X.X.; project administration, X.X.; funding acquisition, Y.Y. All authors have read and agreed to the published version of the manuscript.", please turn to the CRediT taxonomy for the term explanation. Authorship must be limited to those who have contributed substantially to the work reported.

Funding: Please add: "This research received no external funding" or "This research was funded by NAME OF FUNDER grant number XXX." and and "The APC was funded by XXX". Check carefully that the details given are accurate and use the standard spelling of funding agency names at https://search.crossref.org/funding, any errors may affect your future funding.

Institutional Review Board Statement: In this section, please add the Institutional Review Board Statement and approval number for studies involving humans or animals. Please note that the Editorial Office might ask you for further information. Please add "The study was conducted according to the guidelines of the Declaration of Helsinki, and approved by the Institutional Review Board (or Ethics Committee) of NAME OF INSTITUTE (protocol code XXX and date of approval)." OR "Ethical review and approval were waived for this study, due to REASON (please provide a detailed justification)." OR "Not applicable" for studies not involving humans or animals. You might also choose to exclude this statement if the study did not involve humans or animals.

Informed Consent Statement: Any research article describing a study involving humans should contain this statement. Please add "Informed consent was obtained from all subjects involved in the study." OR "Patient consent was waived due to REASON (please provide a detailed justification)." OR "Not applicable" for studies not involving humans. You might also choose to exclude this statement if the study did not involve humans.

Written informed consent for publication must be obtained from participating patients who can be identified (including by the patients themselves). Please state "Written informed consent has been obtained from the patient(s) to publish this paper" if applicable.

Data Availability Statement: In this section, please provide details regarding where data supporting reported results can be found, including links to publicly archived datasets analyzed or generated during the study. Please refer to suggested Data Availability Statements in section "MDPI Research Data Policies" at https://www.mdpi.com/ethics. You might choose to exclude this statement if the study did not report any data.

Acknowledgments: In this section you can acknowledge any support given which is not covered by the author contribution or funding sections. This may include administrative and technical support, or donations in kind (e.g., materials used for experiments).

Conflicts of Interest: Declare conflicts of interest or state "The authors declare no conflict of interest." Authors must identify and declare any personal circumstances or interest that may be perceived as inappropriately influencing the representation or interpretation of reported research results. Any role of the funders in the design of the study; in the collection, analyses or interpretation of data; in the writing of the manuscript, or in the decision to publish the results must be declared in this section. If there is no role, please state "The funders had no role in the design of the study; in the collection, analyses, or interpretation of data; in the writing of the manuscript, or in the decision to publish the results".

References

1. Bažant, Z.P. Size effect in blunt fracture: concrete, rock, metal. *Journal of engineering mechanics* **1984**, *110*, 518–535.
2. Bažant, Z.P.; Planas, J. *Fracture and size effect in concrete and other quasibrittle materials*; CRC press, 1997.
3. Planas, J.; Guinea, G.; Elices, M. Size effect and inverse analysis in concrete fracture. *International Journal of Fracture* **1999**, *95*, 367.
4. Jirásek, M.; Rolshoven, S.; Grassl, P. Size effect on fracture energy induced by non-locality. *International Journal for Numerical and Analytical Methods in Geomechanics* **2004**, *28*, 653–670.
5. Bažant, Z.P.; Yu, Q. Universal size effect law and effect of crack depth on quasi-brittle structure strength. *Journal of engineering mechanics* **2009**, *135*, 78–84.
6. Alberti, M.G.; Gálvez, J.C.; Enfedaque, A.; Carmona, A.; Valverde, C.; Pardo, G. Use of Steel and Polyolefin Fibres in the La Canda Tunnels: Applying MIVES for Assessing Sustainability Evaluation. *Sustainability* **2018**, *10*, 4765.
7. Enfedaque, A.; Alberti, M.G.; Gálvez, J.C.; Rivera, M.; Simón-Talero, J. Can Polyolefin Fibre Reinforced Concrete Improve the Sustainability of a Flyover Bridge? *Sustainability* **2018**, *10*, 4583.
8. di Prisco, M.; Felicetti, R.; Lamperti, M.; Menotti, G. On size effect in tension of SFRC thin plates. *Fracture mechanics of concrete structures* **2004**, *2*, 1075–1082.
9. Yoo, D.Y.; Banthia, N.; Yang, J.M.; Yoon, Y.S. Size effect in normal- and high-strength amorphous metallic and steel fiber reinforced concrete beams. *Construction and Building Materials* **2016**, *121*, 676 – 685. doi:https://doi.org/10.1016/j.conbuildmat.2016.06.040.
10. Picazo, Á.; Alberti, M.G.; Gálvez, J.C.; Enfedaque, A.; Vega, A.C. The Size Effect on Flexural Fracture of Polyolefin Fibre-Reinforced Concrete. *Applied Sciences* **2019**, *9*, 1762.
11. Enfedaque, A.; Alberti, M.; Gálvez, J.; Domingo, J. Numerical simulation of the fracture behaviour of glass fibre reinforced cement. *Construction and Building Materials* **2017**, *136*, 108 – 117. doi:https://doi.org/10.1016/j.conbuildmat.2016.12.130.
12. Alberti, M.; Enfedaque, A.; Gálvez, J.; Reyes, E. Numerical modelling of the fracture of polyolefin fibre reinforced concrete by using a cohesive fracture approach. *Composites Part B: Engineering* **2017**, *111*, 200 – 210. doi:https://doi.org/10.1016/j.compositesb.2016.11.052.
13. Suárez, F.; Gálvez, J.; Enfedaque, A.; Alberti, M. Modelling fracture on polyolefin fibre reinforced concrete specimens subjected to mixed-mode loading. *Engineering Fracture Mechanics* **2019**, *211*, 244 – 253. doi:https://doi.org/10.1016/j.engfracmech.2019.02.018.
14. Enfedaque, A.; Alberti, M.G.; Gálvez, J.C. Influence of Fiber Distribution and Orientation in the Fracture Behavior of Polyolefin Fiber-Reinforced Concrete. *Materials* **2019**, *12*, 220.
15. Alberti, M.; Enfedaque, A.; Gálvez, J. Comparison between polyolefin fibre reinforced vibrated conventional concrete and self-compacting concrete. *Construction and Building Materials* **2015**, *85*, 182 – 194. doi:https://doi.org/10.1016/j.conbuildmat.2015.03.007.
16. European Committee for Standardization. Test method for metallic fibre concrete. Measuring the flexural tensile strength (limit of proportionality (LOP), residual), 2007.
17. Hillerborg, A.; Modéer, M.; Petersson, P.E. Analysis of crack formation and crack growth in concrete by means of fracture mechanics and finite elements. *Cem Concr Res* **1976**, *6*, 773 – 781.
18. Dugdale, D.S. Yielding of steel sheets containing slits. *J Mech Phys Solids* **1960**, *8*, 100–104.
19. Barenblatt, G.I. The mathematical theory of equilibrium cracks in brittle fracture. In *Advances in applied mechanics*; Elsevier, 1962; Vol. 7, pp. 55–129.
20. Sancho, J.; Planas, J.; Cendón, D.; Reyes, E.; Gálvez, J. An embedded crack model for finite element analysis of concrete fracture. *Engineering Fracture Mechanics* **2007**, *74*, 75 – 86. Fracture of Concrete Materials and Structures, doi:https://doi.org/10.1016/j.engfracmech.2006.01.015.
21. Gálvez, J.; Planas, J.; Sancho, J.; Reyes, E.; Cendón, D.; Casati, M. An embedded cohesive crack model for finite element analysis of quasi-brittle materials. *Eng Fract Mech* **2013**, *109*, 369–386.
22. Reyes, E.; Gálvez, J.; Casati, M.; Cendón, D.; Sancho, J.; Planas, J. An embedded cohesive crack model for finite element analysis of brickwork masonry fracture. *Engineering Fracture Mechanics* **2009**, *76*, 1930 – 1944. doi:https://doi.org/10.1016/j.engfracmech.2009.05.002.
23. Smith, M. *ABAQUS/Standard User's Manual, Version 6.9*; Dassault Systèmes Simulia Corp: United States, 2009.
24. Elices, M.; Guinea, G.; Gómez, J.; Planas, J. The cohesive zone model: advantages, limitations and challenges. *Engineering fracture mechanics* **2002**, *69*, 137–163.